1   **Bacteriophage uptake by Eukaryotic cell layers represents a major sink for**

2   **phages during therapy**

3

4   **Authors**

5   Marion C. Bichet[1], Wai Hoe Chin[1], William Richards[1], Yu-Wei Lin[2], Laura Avellaneda-

6   Franco[1], Catherine A. Hernandez[3], Arianna Oddo[4], Oleksandr Chernyavskiy[5], Volker

7   Hilsenstein[5], Adrian Neild[6], Jian Li[2], Nicolas Hans Voelcker[4], Ruzeen Patwa[1] & Jeremy J.

8   Barr[1*]

9   [1] School of Biological Sciences, Monash University, Clayton Campus, VIC, 3800, Australia

10   [2] Biomedicine Discovery Institute and Department of Microbiology, Monash University, Clayton, VIC,

11   Australia

12   [3] Department of Integrative Biology, University of California, Berkeley, Berkeley, CA, USA

13   [4] Faculty of Pharmacy and Pharmaceutical Sciences, Monash University, Parkville Campus, VIC, 3800,

14   Australia

15   [5] Monash Micro Imaging, Monash University, Clayton Campus, VIC, 3800, Australia

16   [6] Department of Mechanical and Aerospace Engineering, Monash University, Clayton Campus, VIC,

17   3800, Australia

18

19   [*]**Corresponding author**

20   Jeremy J. Barr

21   25 Rainforest Walk, School of Biological Sciences, Monash University, Clayton Campus, VIC,

22   3800, Australia

23   jeremy.barr@monash.edu

Bichet et al. 2020

24 Abstract

25   For over 100 years, bacteriophages have been known as viruses that infect bacteria. Yet
26   it is becoming increasingly apparent that bacteriophages, or phages for short, have tropisms
27   outside their bacterial hosts. During phage therapy, high doses of phages are directly
28   administered and disseminated throughout the body, facilitating broad interactions with
29   eukaryotic cells. Using live cell imaging across a range of cell lines we demonstrate that cell
30   type plays a major role in phage internalisation and that smaller phages (< 100 nm) are
31   internalised at higher rates. Uptake rates were validated under physiological shear stress
32   conditions using a microfluidic device that mimics the shear stress to which endothelial cells
33   are exposed to in the human body. Phages were found to rapidly adhere to eukaryotic cell
34   layers, with adherent phages being subsequently internalised by macropinocytosis and
35   functional phages accumulating and stably persisting intracellularly. Finally, we incorporate
36   these results into an established pharmacokinetic model demonstrating the potential impact of
37   phage accumulation by these cell layers, which represents a major sink for circulating phages
38   in the body. Understanding these interactions will have important implications on innate
39   immune responses, phage pharmacokinetics, and the efficacy of phage therapy.
40

Introduction

41   Phages, short for bacteriophages, are viruses that infect bacteria and are the most abundant life

42   form on the planet (1–3). Phages are found ubiquitously in the environment and are a major

43   contributor to global genetic diversity (4–6). Our bodies harbour a large number of phages,

44   and, together with their bacterial hosts, they constitute a key component of our gut microbiome

45   (7). The gut carries the largest aggregation of phages in the body, with an estimated 2×10^{12}

46   phages present in the average human colon (4,8,9). These phages are constantly interacting

47   with gut bacteria, as well as the epithelial cell layers of the gut (10). Phages are detected in the

48   circulatory systems of the body, suggesting they are capable of translocating from the gut and

49   penetrating throughout the body (8,11). Once past the gut barrier phages are able to penetrate

50   cell layers and major organs of the body; being found in classically sterile regions such as the

51   blood, serum, organs and even the brain (8,10–19). Numerous mechanisms pertaining to the

52   transport of phages across epithelial barriers have been proposed (11,16), including the 'leaky

53   gut' where phages bypass cell barriers at sites of damage and inflammation (20,21), and

54   receptor-mediated endocytosis (22,23). Recently, a non-specific mechanism for phage uptake

55   and transport across epithelial cell layers was proposed by Nguyen and colleagues, whereby

56   epithelial cells uptake phages via macropinocytosis and preferentially transcytose phages from

57   the apical surface toward the basolateral side of the cell (8,24). Macropinocytosis is a broad

58   mechanism describing the enclosure of media within ruffles in cells' membrane, prior to

59   internalising the media, and any phages it may contain, within the cells. Despite their

60   prevalence in the human body, phage's capacity to interact with and influence eukaryotic cells

61   remains largely unknown. These interactions can have important implications during phage

62   therapy.

63

64   Phage therapy is a promising alternative to treat pathogenic bacterial infections. In Eastern

65   Europe, phage therapy was widely used since its discovery in 1917 (1), whereas in Western

66   countries, phage therapy was largely abandoned in favour of antibiotics (25–28). However,

67   with the rise of antimicrobial resistance as one of the greatest threats to human health, phage

68   therapy is being re-established as a potential treatment option for difficult-to-treat, antibiotic

69   resistant, bacterial infections (25). In order for phage therapy to be effective, phages must first

70   be administered to the site of infection. Administration routes include, intravenous (IV) or

71   intraperitoneal (IP) to treat septicaemia; orally to treat gastrointestinal infections; intranasal or

72   inhalation to treat respiratory infections; or topically for cutaneous infections (29,30). The

Bichet et al. 2020

74   administration route and bioavailability of phages needs to be carefully taken into account in
75   order to achieve favourable efficacy *in vivo*.

76

77   In contrast to conventional drugs, phages are unique therapeutic agents capable of self-
78   replicating and maintaining titres in the body (30–33). As such, there is a lack of knowledge
79   regarding phage pharmacokinetics and pharmacodynamics (31). Following administration, two
80   major pharmacokinetic factors important for the efficacy of phage therapy are accessibility and
81   clearance. First, natural barriers such as cell layers and mucus can decrease accessibility of
82   phages to sites of infection, thereby necessitating the administration of higher doses to achieve
83   a favourable therapeutic effect. Second, phage clearance has been reported to occur rapidly;
84   sometimes within just minutes to hours following parenteral administration in animal models
85   and patients (14,34–40). Phage clearance within the body is thought to be mediated by three
86   main components: 1) Phagocytic cells (41), 2) The Mononuclear Phagocytic System (MPS;
87   which was also previously called the reticuloendothelial system, or RES) which includes the
88   liver and spleen that filter out and remove phages from circulation (42), and 3) Phage
89   neutralizing antibodies, although it is still unclear how effective and rapidly produced these
90   anti-phage antibodies are (31,43). Due to these complications, it is difficult to predict how
91   phages will behave in the body when administered and ultimately whether phage therapy will
92   be successful.

93

94   One underexplored aspect of phage therapy is the non-specific interactions between phages
95   and the cell layers of the body. During therapy, large quantities of phage monocultures or
96   cocktails are administered to patients in order to maintain a killing titre to combat a bacterial
97   infection. Once within the body, these phages can have very short half-lives and are actively
98   removed or inactivated by the body (38–40,44). Following administration during phage
99   therapy, epithelial and endothelial cell layers are amongst the first and most abundant phage-
100   eukaryote interactions. Here, we present new insights into phage-mammalian cell adherence,
101   uptake, and trafficking, via *in vitro* tissue culture cell layers. Our results suggest that cell layers
102   of the human body represent a major and unaccounted sink for exogenously administered
103   phages. Put within the context of phage therapy, the interaction between eukaryotic cells and
104   exogenous phages have important implications for phage administration, dosing, and
105   pharmacokinetics.

106

Bichet et al. 2020

107   **Results**

108   **The rate of phage uptake varies depending on the cell type.** To better understand phage-

109   eukaryote interactions, we used seven *in vitro* tissue culture cell lines that were selected to be

110   broadly representative of different tissues types within the body, and examined their

111   interactions with ultrapure high titre monocultures of T4 phage. Using real time live-cell

112   imaging on a confocal microscope with a sensitive hybrid detector (HyD), we visualised the

113   interaction and subsequent internalisation of phage particles within eukaryotic cells. Cells were

114   first grown on glass bottom slides for two days to generate an ~ 80% confluent cell layer,

115   followed by fluorescence staining of the nucleus and plasma membrane. T4 phages were

116   prepared using the Phage-on-Tap method (45), labelled using SYBR-Gold, subsequently

117   washed to remove residual stain, and then directly applied to cell layers observed using live

118   cell imaging.

119

120   Phages were visualised in real time being engulfed and trafficked through all seven of the

121   different cell lines over a two-hour period (Fig. 1a and Supplemental movies SM1-7). The cell

122   types tested include: epithelial cells - HeLa, A549 and HT29, from the cervix, lung and colon,

123   respectively; fibroblast cells - MDCK-I and BJ, from dog kidney and human skin, respectively;

124   the endothelial cell line - HUVEC from umbilical vein; and monocyte-induced macrophages -

125   THP-1 cells (Fig. 1b). The increase in green fluorescence over time corresponds to the uptake

126   and accumulation of fluorescently labelled T4 phages by the cells. We saw the first evidence

127   of phage accumulation within cells occurring around 30 minutes, with continued accumulation

128   over the following 90 minutes.

129

130   We observed large variation in the uptake of phages across the seven cell types investigated.

131   To quantify this, cells containing intracellular phages were manually counted and compared

132   with the total number of cells in the field of view (FOV) at the two-hour time point for each

133   replicate. Cells were then categorised as either high, intermediate, or low phage-uptake using

134   univariate clustering analysis (Fig. 1c and Supplemental Fig. 1) (46). A549 lung epithelial cells

135   showed the highest accumulation of phages, with a median of cells containing fluorescently-

136   labelled phages at the two-hour time point of 99% (± 2%, mean ± standard deviation [SD];

137   Field of View [FOV] n = 8; coefficient of variation [CV] = 2%). Next, HUVEC, MDCK-1,

138   and HeLa cells, representing endothelial, fibroblast and epithelial cell types all showed

139   intermediate levels of phage accumulation at the two hour time point, with medians of 44% (±

Bichet et al. 2020

140   34% SD; FOV $n = 10$; CV = 63%), 51% ($\pm$ 26% SD; FOV $n = 4$; CV = 54%), and 41% ($\pm$ 18%

141   SD; FOV $n = 7$; CV = 42%) of phage-positive cells, respectively. Finally, THP-1, HT29, and

142   BJ cells, representing macrophages, epithelial and fibroblast all showed little to no

143   accumulation with medians of 0% ($\pm$ 11% SD; FOV $n = 9$; CV = 155%), 0% ($\pm$ 0.5% SD; FOV

144    $n = 4$; CV = 200%), and 0% ($\pm$ 0% SD; FOV $n = 4$; CV = 0%) phage-positive cells at two

145   hours, respectively. We further quantified the rate at which cells internalised phages by

146   manually counting the number of cells per frame of interest containing fluorescently-labelled

147   phages for each of the field of view per cell lines (Fig. 1d). Most cells showed large variability

148   in the uptake rate over the two-hour period. For A549 cells, which had the highest accumulation

149   of phages, we saw large variation in the rate of uptake, with a median of 27% ($\pm$ 36% SD; FOV

150    $n = 6$; CV = 83%) of cells that contained phages at one hour of incubation compared to 100%

151   ($\pm$ 0% SD; FOV $n = 6$; CV = 0%) of cells at two hours. Comparatively, HUVECs, which were

152   classified as intermediate accumulation of phages showed extensive variability in their uptake

153   rates, with a median of 12% ($\pm$ 41% SD, FOV $n = 8$; CV = 116%) and 46% ($\pm$ 35% SD; FOV

154    $n = 8$; CV = 60%) of cells containing phages at one and two hours, respectively.

155

156   To confirm that phages were internalised and not simply attached to the cell surface, we created

157   a three-dimensional (3D) reconstruction using a Z stack to visualise the intracellular

158   localisation of phages. After the live cell imaging of MDCK-I cells incubated with

159   fluorescently-labelled T4 phages for one hour (Supplemental movie SM8), we acquired a high-

160   resolution Z stack image of one chosen field of view. We reconstituted the 3D volume of the

161   cell to visualise phage repartition in the cytoplasm (Fig. 2 top left corner and Supplemental

162   movie SM9). Finally, we looked at the localization of phages in 3D using the XY cross section

163   (Fig. 2). The 3D reconstruction of the cell confirmed that phages internalized by the cells

164   (visualised as green fluorescent particles) lie in the same focal plane as the nucleus (Fig. 2).

165   Phages were distributed throughout the cell cytoplasm and appeared to be localised within

166   membrane-bound vesicles surrounding the nucleus.

167

Bichet et al. 2020

Plasma membrane, nucleus, phage DNA
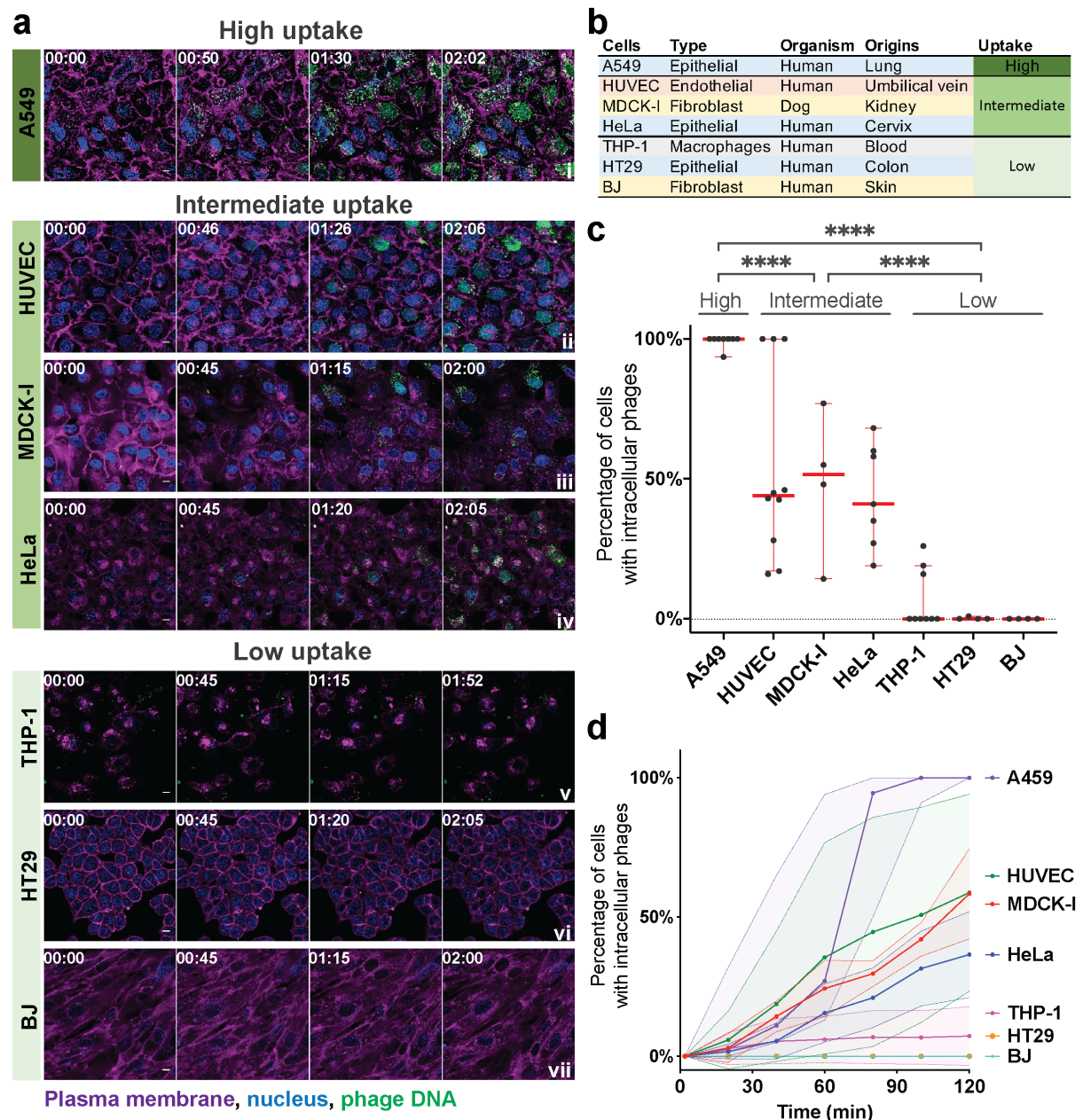
Figure 1. Uptake and internalisation of phages varies across cell type. (**a**) T4 phage was fluorescently labelled, applied to different cell lines and incubated for two hours on a glass bottom slide. Cells were stained with Hoechst 33342 nucleus stain (blue), CellMask plasma membrane stain (magenta) and T4 phages labelled with SYBR-Gold DNA-complexing stain (green). Using real-time microscopy, one image was acquired every two minutes. Scale bar: 10 μm; Timing: hours:minutes. (**b**) Table of cell lines used in this study, their cell type, organism, organ origins and category of uptake. Cells lines are ranked as high, intermediate, and low uptake. (**c**) Percentage of cells containing intracellular phages at the two-hour time point. Scatter plots show medians of percentage of cells with intracellular phages; error bars represent 95% confidence intervals; each dot represents one Field of View (FOV). Cells lines are ranked as high, intermediate and low uptake. P-values between the different groups calculated from a one-way ANOVA, shown as stars (F (2, 43) = 71.23; P < 0.0001: ****). (**d**) Percentage of cells containing phages represented across time. For each video the number of cells with and without intracellular phages in a FOV were manually counted every ten minutes (A549 $n = 6$; HUVEC $n = 8$; MDCK-I $n = 3$; HeLa $n = 6$; THP-1 $n = 8$; HT29 $n = 3$; BJ $n = 3$).

7

Bichet et al. 2020

185 Curve plots show medians of percentage of cells with intracellular phages; error bars represent
186 95% confidence intervals in the shaded area for each curve; each point represents one video
187 over time.
188
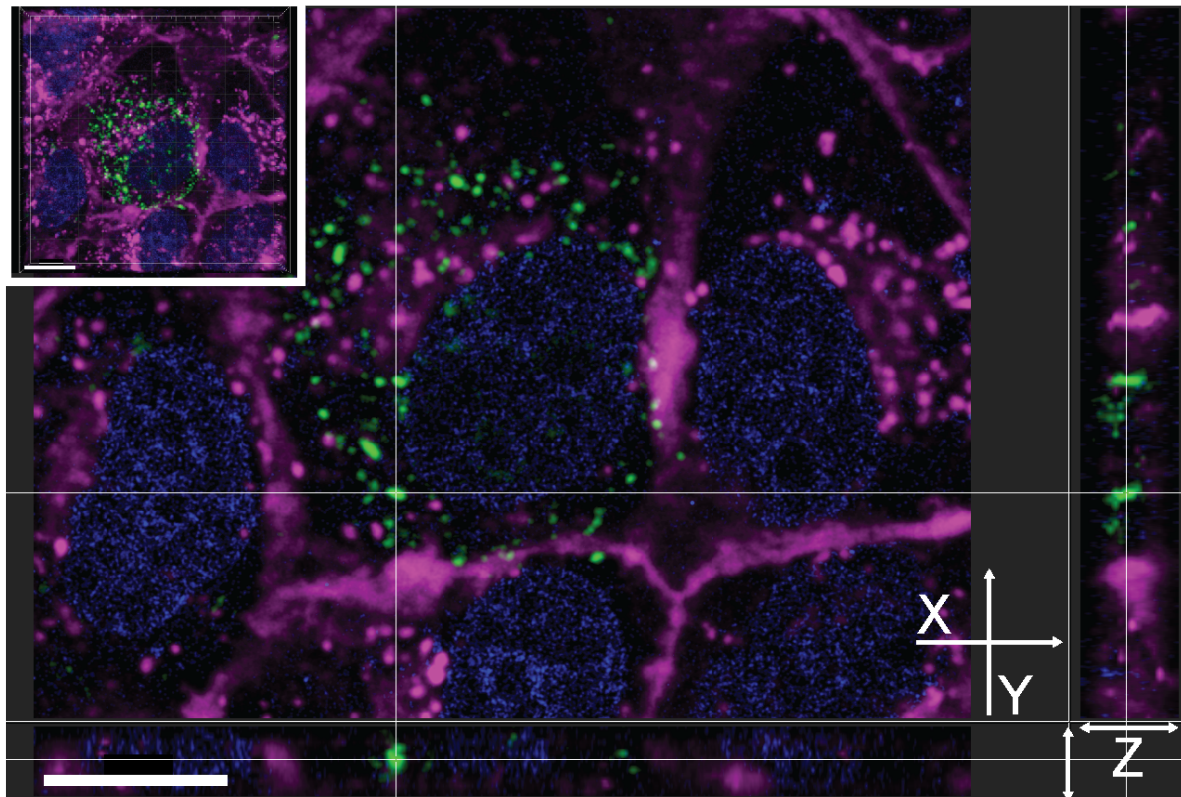
Plasma membrane, nucleus, phage DNA

189
190

191 **Figure 2. 3D reconstruction of intracellular phages.** MDCK-I cells were incubated for an
192 hour with T4 phages on glass bottom slide before acquisition of a high-resolution Z stack to
193 visualise phage dispersion inside of cells. Cells were stained with Hoechst 33342 nucleus stain
194 (blue), CellMask plasma membrane stain (magenta) and T4 phages labelled with SYBR-Gold
195 DNA-complexing stain (green). Images were acquired in real-time on live cells. XY cross
196 section made using Imaris software with an embedded 3D projection of the cell in the top left
197 corner of the image. The cross in the centre of the image shows a cluster of internalised phages
198 with its repartition in the Z dimension (depth) of the image represented in the X and Y sides
199 views. Scale bar: 10 μm.
200

Bichet et al. 2020

Phage uptake occurs at comparable rates under both static and flow conditions. The previous experiments were all conducted under static conditions, where phages were directly applied to the cell culture media and phage-cell encounters driven purely by diffusion. However, in the context of phage therapy, phages administered to the body are likely to encounter dynamic environments and active fluid flow, such as in the circulatory and lymphatic system. These dynamic conditions may lead to increased phage-cell encounter rates or altered cellular uptake (47–52). We investigated whether phage uptake rates under static conditions were comparable with uptake rates under fluid flow and shear conditions that mimic the circulatory systems of the body (Fig. 3a). We chose HUVECs to use in our flow experiment for two main reasons, the first one is that they are part of the intermediate uptake group determined in our first figure and are not part of one of the two other extremes. Secondly, HUVECs are endothelial cells and would be amongst the first type of cells to be in contact with circulating phages in the human body. Using an in-house fabricated microfluidic device mounted on a glass coverslip adapted for confocal microscopy (53,54), we seeded the device with HUVECs and incubated it under static conditions for 12 hours to ensure sufficient cellular attachment to the subtract. Cell layers were allowed to establish within the device under a low flow rate of 0.66 µl/min for one day, before increasing to a final flow rate of 8 µl/min until cells reached confluency. Physiological shear stress values observed in the human body ranges from 0.1 dyne/cm^2 in the microcirculation, reaching higher rates of 50 dyne/cm^2 found in larger circulatory vessels (55–59). Due to the volumes of media and quantity of phages applied to the chip, we chose a flow rate of 8 µl/min, which is equivalent to a shear stress of 0.1 dyne/cm^2 in our chip and was at the lower end of physiological circulatory range (Supplemental Table 1). We perfused the chips with media containing 10^9 phages/ml, with phage uptake visualised as previously described at two and 18 hours timepoints. Even though the volumes and quantity of phages seen by the cell layer in the static (200 µl) and flow (960 µl) conditions are different, we still observe similar rates of T4 phage uptake after two hours (Fig. 1a & 3b. ii and Supplemental Fig. 3). After 18 hours incubation under shear stress, we observed a significant increase in the fluorescence intensity compared with two hours incubation (unpaired t-test, P < 0.001) (Supplemental Fig. 3).
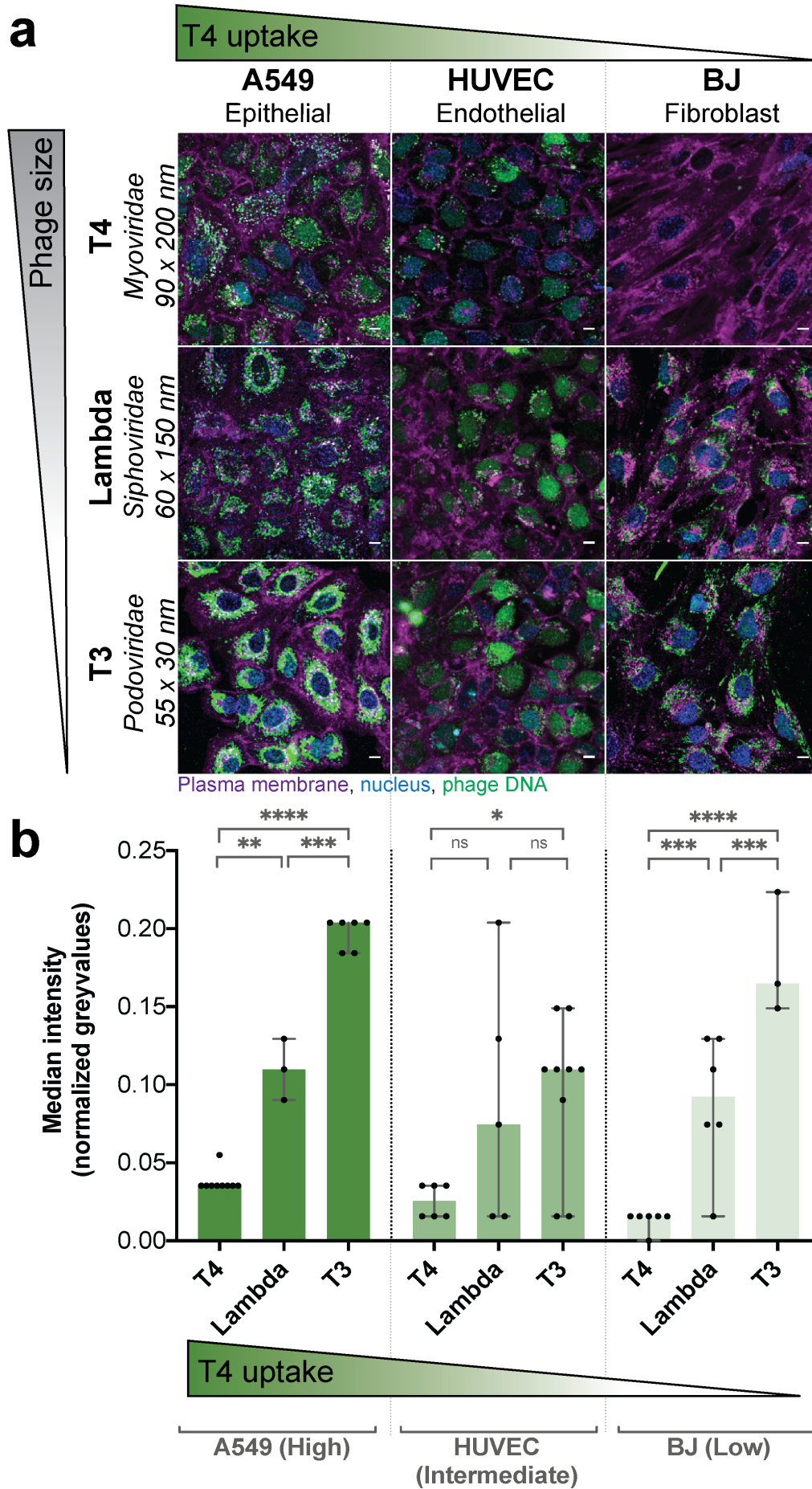
Bichet et al. 2020
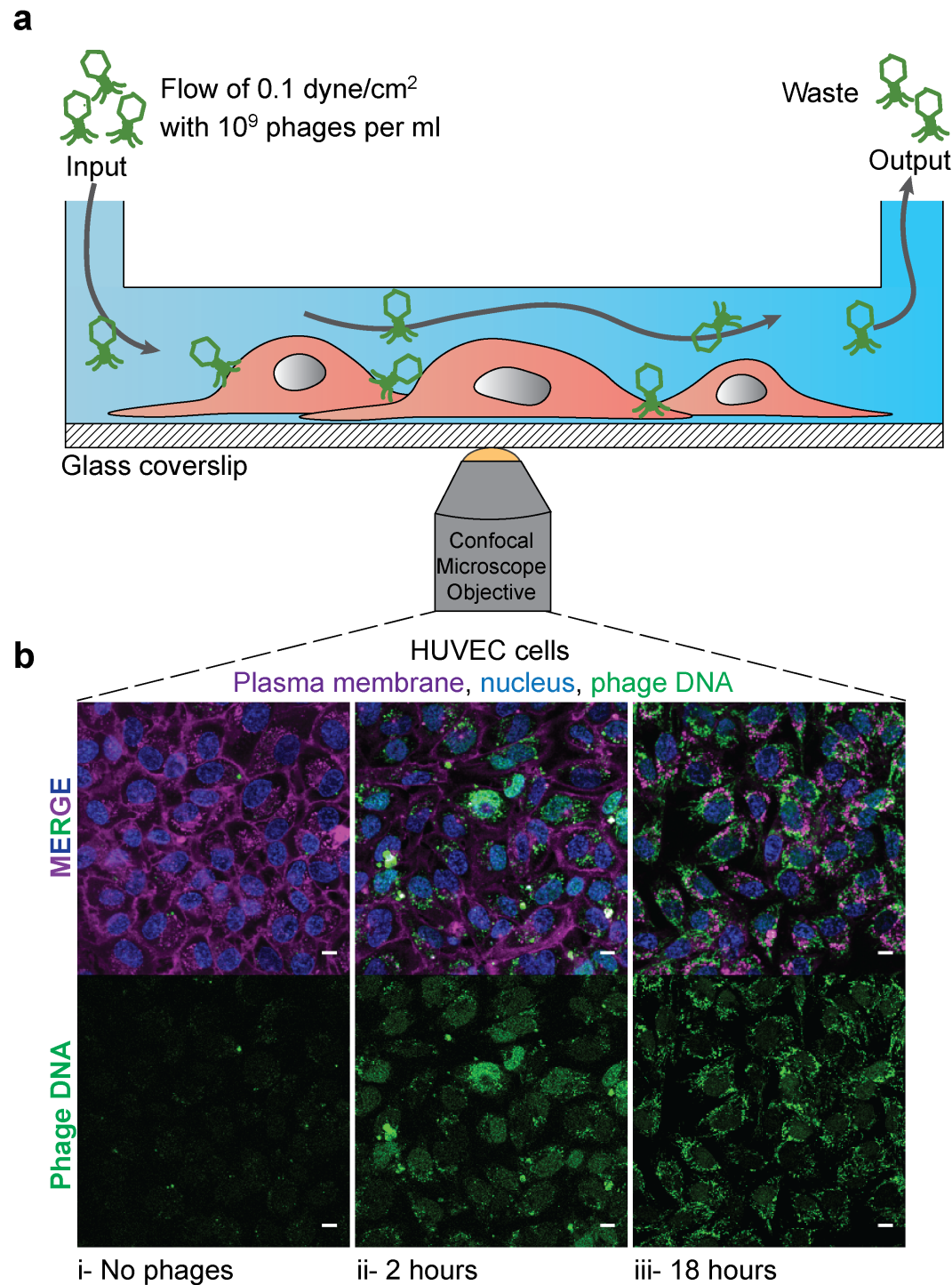
Figure 3. Uptake of phages under fluid flow and shear stress. T4 phage was applied to HUVECs within a microfluidic channel of a microfluidic device under a shear stress of 0.1 dyne/cm² for two or 18 hours with images collected via real-time microscopy images. **(a)** Schematic of the microchannel showing the flow from one port of the channel to the other side of the channel where the waste was collected. **(b)** Cells were stained with nucleus stain (blue), plasma membrane stain (magenta) and T4 phages labelled with DNA-complexing stain (green). Control cells without phages i). Cells were incubated under a constant flow of phages at a rate of 8 μL/min equivalent to a shear stress of 0.1 dyne/cm² for either ii) two or iii) 18 hours. Scale bar:10 μm.

10

242   **Phage size affects intracellular uptake.** Next, we looked at the effect of phage size on the

243   rate of cellular uptake. We chose three *Escherichia coli* infecting phages; T4 phage from the

244   *Myoviridae* family, measuring 90 nm wide and 200 nm long with a contractile tail; Lambda

245   phage from the *Siphoviridae* family, measuring 60 nm wide and 150 nm long with a non-

246   contractile tail; and T3 phage from the *Podoviridae* family, measuring 55 nm wide and 30 nm

247   long with a small non-contractile tail. We tested these phages against three cell lines

248   representative of high, intermediate, and low rates of uptake (Fig. 1c); A549 cells with a high

249   rate of uptake, HUVECs with an intermediate rate, and BJ cells with a low rate. We incubated

250   phages with the cell layers for two hours, acquiring images every two minutes (Supplemental

251   movies SM1-2, 7, 10-15), with the final time point represented in Fig. 4a. The first row of

252   images shows clear differences in T4 phage uptake between the three cell lines (Fig. 4a).

253   However, when we applied the smaller sized Lambda and T3 phages to the three cells lines,

254   we saw a large increase in the uptake of both phages compared with T4. This was particularly

255   evident in the BJ cell line, which had effectively no T4 phage update over a two-hour period

256   but nonetheless, demonstrated increased uptake of the smaller sized Lambda and T3 phage.

257   We quantified phage uptake across phage size and cell type using a pipeline built with

258   CellProfiler software (60) (see methods) to analyse the median grayvalue intensity in the cell

259   region (median over all pixels in FOV marked as cells) as a proxy for fluorescence intensity of

260   phage (Figure 4). For T3 phage, the smallest phage of the three tested, we observed the highest

261   rate of uptake across the three cell lines (ANOVA one way, $F_{(2, 45)}$ = 71,32; $P < 0.0001$).

262   This was especially evident for the BJ cell line where the median intensity of the phage

263   fluorescence signal increased from a median of 0.01 normalised grey value with T4 phage ($\pm$

264   0.006 SD; FOV n = 6; CV = 49%) up to 0.09 with Lambda ($\pm$ 0.04 SD; FOV n = 6; CV =

265   49%), and finally to 0.16 with T3 phage ($\pm$ 0.04 SD; FOV n = 3; CV = 22%) (Fig. 4b). Based

266   on our microscopy results, we suggest that smaller sized phages broadly increase the rate of

267   cellular uptake, and that these effects were more pronounced in our intermediate and low

268   uptake cell lines.

269

Bichet et al. 2020

Plasma membrane, nucleus, phage DNA

270

Bichet et al. 2020

271 **Figure 4. Cellular uptake of differing phage particle sizes.** Real-time microscopy images
272 showing differential uptake of phages based on particle size. One representative cell line from
273 each of the three high, intermediate, and low uptake groups were picked. **(a)** Images were
274 acquired in real-time. Cells were stained with Hoechst 33342 nucleus stain (blue), CellMask
275 plasma membrane stain (magenta) and T4 phages labelled with SYBR-Gold DNA-complexing
276 stain (green). Three cell lines used; A549, HUVEC and BJ, with the three phages; T4, Lambda,
277 and T3. Green gradient shows the qualitative increase in T4 phage uptake shown in Figure 1C.
278 Grey gradient shows qualitative decrease in sizes of phages T4 (90×200 nm), Lambda ($60 \times$
279 150 nm), and T3 (55×30 nm). Scale bar $= 10$ μm. The image shown is the last image at two-
280 hour acquisition. **(b)** Fluorescence intensity of the "phage object" area in normalized grey
281 values quantified from the CellProfiler software of the phage channel fluorescence at the two-
282 hour time point (A549 - T4 $n = 9$; A549 - Lambda $n = 3$; A549 - T3 $n = 6$; HUVEC - T4 $n = 6$;
283 HUVEC - Lambda $n = 3$; HUVEC - T3 $n = 6$; BJ - T4 $n = 6$; BJ - Lambda $n = 6$; BJ - T3 $n =$
284 3). Scatter plots show medians over all pixels in FOV marked as cells; error bars represent 95%
285 confidence intervals; each point represents one FOV. P-values calculated from a one-way
286 ANOVA ($P < 0.0001$: ****; $P < 0.05$: *; ns: non-significant).
287

13

Bichet et al. 2020

288 **Phages rapidly adhere to eukaryotic cells, resulting in inactivation and uptake.** We
289 demonstrate that phages have different rates of cellular uptake depending on both cell type and
290 the size of phages. Yet whether these phages remained functional, or if they were inactivated
291 by the cellular uptake and trafficking pathways remains unclear. To answer this, we quantified
292 the number intracellular phages using two methods; classic plaque formation unit (PFU) assays
293 and Droplet Digital PCR (ddPCR). Briefly, PFUs allowed us to quantify the number of active
294 or functional phages present within the cells, while ddPCR quantified the absolute number of
295 phage DNA genome copies present in the sample. We evaluated the accuracy of the two
296 techniques with a dilution series of our initial phage sample from 10^9 to 10^2 phages per ml
297 using PFU and ddPCR (Supplemental Fig. 4). Subtracting active phages (PFU) from phage
298 DNA genome copies (ddPCR) enabled us to quantify the proportion of phages inactivated or
299 damaged during cellular uptake and trafficking, as these damaged phages are no longer able to
300 infect their bacterial host and therefore will only be detected by ddPCR.
301
302 In order to differentiate between intracellular phages and those adhered to the cell surface, we
303 incubated cells with T4 phages ($\sim 10^9$ per ml) for two different periods of time: 30 seconds,
304 which is too short for phage internalisation; and 18 hours, to maximise the number of
305 internalised phages. After incubation at each time point, cells were extensively washed to
306 remove non-adherent phages, lysed, and phages quantified by both PFU and ddPCR (Fig. 5a).
307 We compared the same representative cell types previously used for high, intermediate, and
308 low uptake cell lines (Fig. 5b). For all three cell lines, we saw between 90 and 2200 active
309 phages (PFU) per ml adhered to the cells within 30 second treatment, with a median of 625
310 phages/ml ($\pm$ 420 SD; $n = 6$; CV = 60.1%), 325 phages/ml ($\pm$ 300 SD; $n = 6$; CV = 76.6%) and
311 250 phages/ml ($\pm$ 850 SD; $n = 6$; CV = 114%) for A549, HUVEC and BJ cells, respectively,
312 suggesting a small, yet persistent number of phages rapidly adhere to the cell layers. After 18
313 hours of incubation, we saw a large increase in the number of functional phages associated
314 with the cells, with between 1.1×10^4 to 3.1×10^6 phages per ml accumulating within the three
315 cell lines. Looking across the different cell lines, we see the highest accumulation of phages in
316 the intermediate uptake cells, with a median of 5×10^5 phages/ml ($\pm$ 6.4×10^5 SD; $n = 9$; CV
317 = 85.7%) followed by the high and low uptake with medians respectively of 1.2×10^5
318 phages/ml ($\pm$ 8.4×10^4 SD; $n = 9$; CV = 65.7%) and 5×10^4 phages/ml ($\pm$ 1.4×10^6 SD; $n = 9$;
319 CV = 144.3%), although there were no significant difference between the three cell lines (P >
320 0.1, ANOVA one way). We note that the BJ cell line, which showed the lowest rate of uptake

14

321 observed via microscopy (Figure 1), still accumulated active phages over prolonged periods of

322 time with non-significant differences of active phages at 18 hours observed with two other cell

323 lines (unpaired t-test, two tailed, P > 0.08 with A549 and P > 0.6 with HUVEC).

324

325 Surprisingly, when looking at ddPCR results, we see an increase in phage DNA associated with

326 the 30 second treatment in all cell lines, with between 3.9×10^2 and 2.7×10^4 DNA genome

327 copies per ml persisting. When quantifying the inactivated phages at 30 second treatment,

328 which was calculated as the difference in DNA genome copies and PFU, we observe between

329 7×10^1 and 2.7×10^4 inactivated phages per ml. These results suggest that; 1) phages rapidly

330 adhere to eukaryotic cell layers, with a portion of these phages being inactivated, 2) longer

331 incubation time allows for adhered phages to be internalised and accumulate inside of the cells,

332 and 3) that the majority of internalised phage particles remain active and stably persist within

333 the cells for up to 18 hours.

334

Bichet et al. 2020
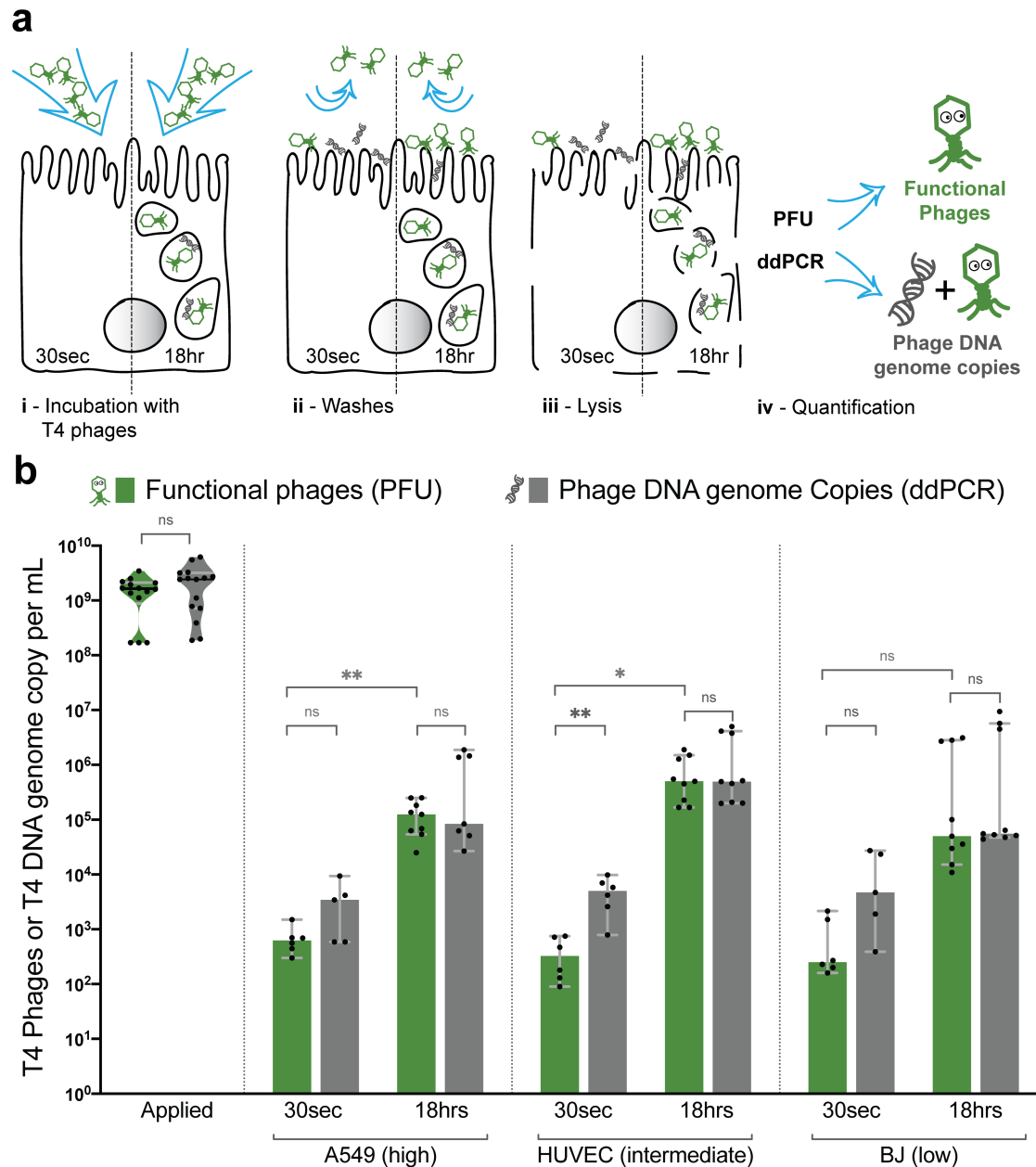
Figure 5. Quantifying adherence and internalisation of phages and their activity. Applied T4 phages were quantified using both traditional plaque assays (PFUs) and Digital Droplet PCR (ddPCR), across three different cell-lines: A549, HUVEC and BJ, representative of the high, intermediate, or low phage uptake. Phages were applied to cells for either 30 seconds as an adherence control, or for 18 hours to saturate phage uptake. (**a**) Schematic representation of the experiment showing steps taken to obtain the samples with two incubation times: 30 seconds or 18 hours. Active or functional phages are represented in green and phage DNA or inactive phages are represented in grey; (i) Incubation of phages with cells, (ii) Extensive washing of cells to remove non-adherent phages, (iii) Chemical and mechanical cell lysis, and (iv) Quantification of the active and total phages via PFU and ddPCR. (**b**) Active T4 phages in green quantified by PFU and in grey the total number of T4 phage DNA genome copies per sample quantified by ddPCR, including both active and inactive phages. Scatter plots show medians of phages or DNA genome copies per mL; error bars represent 95% confidence intervals; each point represents one sample. P-values calculated from an unpaired t-test between each pair (P < 0.001: ***; P < 0.01: **; P < 0.05: *; ns: non-significant).

16

352   **Phage inactivation and internalisation influences pharmacokinetics.** A key underexplored
353   aspect of phage pharmacokinetics (PK) are the non-specific interactions between phages and
354   the epithelial and endothelial cell layers of the body. To address this, we integrated our
355   experimental data (Fig. 5) with an established PK model for phage administration in a rats (38).
356   The model was established from a single-dose PK study performed in healthy rats, following
357   an intravenous bolus of phages. The phage disposition in blood was well characterised using a
358   standard three-compartment PK model (38). In order to evaluate the impact of phage
359   inactivation and internalisation by eukaryotic cells on phage distribution, a fourth-compartment
360   was added to the existing model, representing the epi- and endothelial cell layers (Fig. 6a).
361   Deterministic simulations were subsequently performed with the previously estimated PK
362   parameters (38) and the first-order inactivation constant estimated from our *in vitro* data
363   (ddPCR). Inactivation rate constant was calculated using both the 30 seconds- and 18 hours-
364   derived constants, as a representative of both the rapid and prolonged phage accumulation by
365   cell layers (Fig. 6b, supplemental data SD2, SD3 and table 5). Deterministic simulations were
366   performed at an IV bolus dose of 10^9 phages. With the inactivation rate constant calculated
367   using 30 second data, complete removal of phages was noted as short as three hours. This is
368   consistent with the 30 second *in vitro* data, in which rapid inactivation was observed.
369   Comparatively, using the inactivation rate constant calculated using the 18 hours data, an initial
370   rapid decay of circulating phages, followed by a longer tail and phage persistence in the blood
371   was observed for up to 32 hours. These two models represent two extremes of rapid and
372   prolonged phage accumulation by cell layers, highlighting the potential impact of these cellular
373   mechanisms on phage disposition. Further studies characterising both the affinity of phage–
374   eukaryotic interactions and their influence on PK are needed for better clinical translation.
375

Bichet et al. 2020
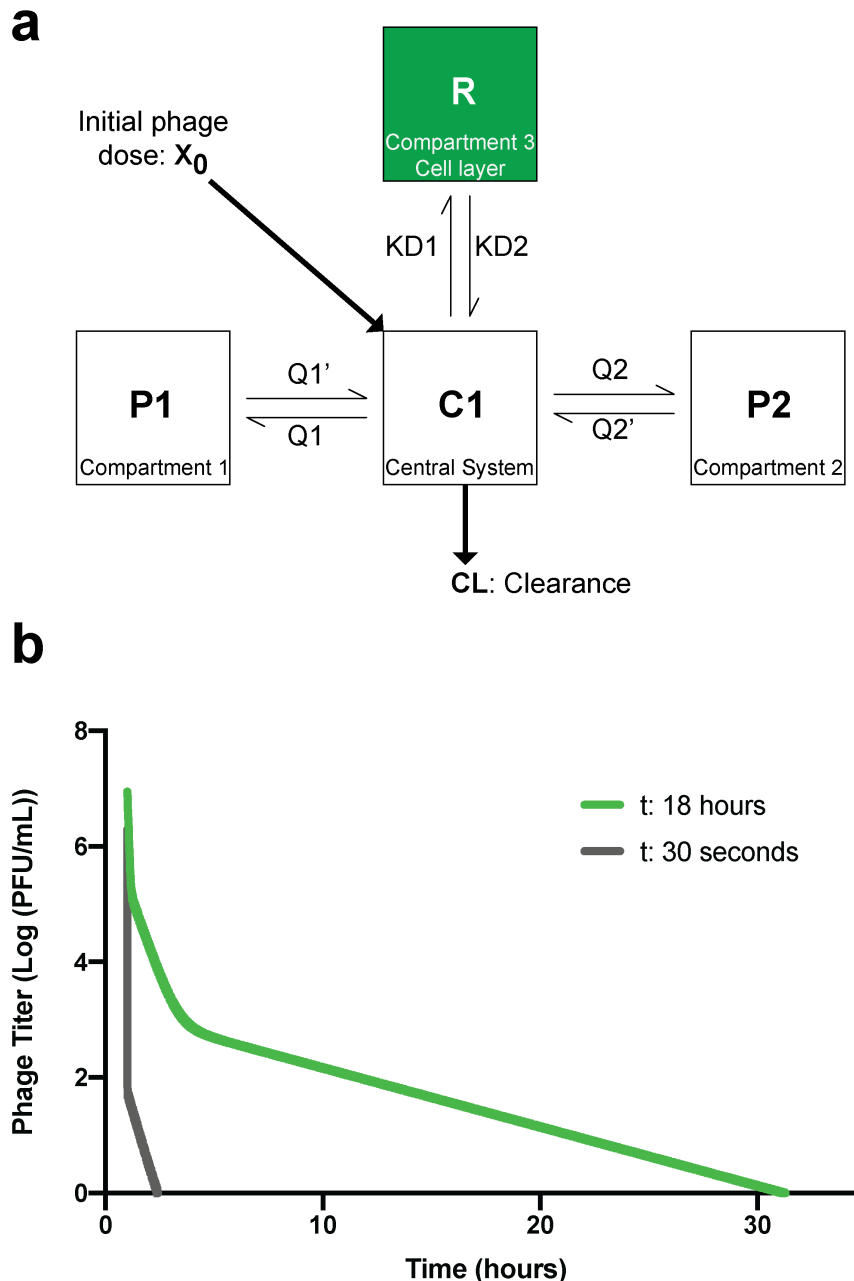
Figure 6. Pharmacokinetic (PK) model of inactivation and internalisation of phages by eukaryotic cell layers. Extrapolation of *in vitro* results were fit to a rat model of phage decay at an initial dose of 10^9 phages. **(a)** Schematic of the standard 3-compartments model with an additional inactivation compartment. X_0, the initial dose of phages and CL phage total body clearance. C1, the central compartment representing the central system (*i.e.,* the blood). P1 and P2 compartments represent various organs or tissues participating in phage decay. R, the new compartment representing *in vitro* cell layers as a major sink of phages. Q1 and Q2 are intercompartmental clearance one and two, respectively. KD1 is the first order inactivation constant and KD2 is the first order reactivation constant (assumed to be zero in our model). **(b)** Graph representing the decay of phages per central volume of distribution over time calculated with *in vitro* data using an R model with an integration step of 0.001. First order for the 30 seconds graph is of 1511 1/h/rat and for the 18 hours the first order is of 0.44 1/h/rat calculated from the geometric mean of ddPCR data (calculation in supplemental table 5).

18

Bichet et al. 2020

391 **Discussion**

392 Phage therapy is one of the more promising solutions in the fight against antibiotic resistance

393 (25). However, the effective use of phages as a treatment against multi-drug resistant bacterial

394 pathogens remains a major challenge to successfully and reproducibly implement. Our

395 understanding of the interactions between bacteriophages and eukaryotic cells may have

396 important implications and impacts for the success of phage therapy. In this article, we

397 investigate the interactions between phages and *in vitro* tissue culture cell layers. We

398 demonstrate that cell type plays a major role in the uptake process of phages, with individual

399 cells taking up phages at different rates, even amongst the same cell types (e.g., epithelial,

400 endothelial, etc.). Uptake rates were validated under shear stress conditions using a

401 microfluidic device that mimics the shear stress to which endothelial cells are exposed to *in*

402 *vivo* (61,62), and shown to be comparable with static conditions. Using live cell imaging we

403 show that phages accumulate within cells over time and that smaller phages are internalised at

404 higher rates than larger phages. Phages were found to rapidly adhere to eukaryotic cells, with

405 adherent phages being internalised by macropinocytosis over the following 18 hours of

406 incubation, with functional phages accumulating and stably persisting within the cells. Finally,

407 we incorporate our results into an established pharmacokinetic (PK) model (38), demonstrating

408 the potential impact of phage accumulation by epithelial and endothelial cell layers, which

409 represent an unaccounted sink of phages within the body.

410

411 The mechanism of non-specific phage uptake by *in vitro* tissue culture cell lines was previously

412 demonstrated to occur via macropinocytosis (8). Cell types have been reported to have differing

413 basal rates of macropinocytosis depending on their function and location within the body (24),

414 thereby influencing their rate of phage uptake. The macropinosome plays further roles in the

415 presentation of antigens for pattern recognition receptors located in other organelles, and in the

416 activation of innate immune responses (63). The fate of phages within the macropinosome is

417 still unknown. It is clear phages accumulate within the macropinosomes over time, but whether

418 they are subsequently degraded by the endosomal/lysosomal system, or recycled and fused

419 back with the plasma membrane remains to be investigated (24). Here we propose that, within

420 seconds, phages rapidly adhere to the eukaryotic cell membrane. Secondly, this adherence

421 leads to an internalisation of phages via non-specific macropinocytosis. Thirdly, this allows for

422 the steady accumulation of phages within the macropinosomes and cell over time. Further

423 research is required to probe the specific mechanisms of phage adherence, uptake, and the

424 cellular mechanisms that govern the trafficking of phages within cells (64,65).

425

426   Using three different phages, from different families, with different sizes, we were able to show

427   an effect of phage size on the rate of uptake across three different cell lines. Using real-time

428   microscopy, we demonstrate that the smaller sized phage particles had increased rates of

429   uptake, especially in low uptake cell lines. One hypothesis for the increased uptake of smaller

430   sized phages, may simply be the result of an increased number of particles capable of

431   interacting with actin-mediated ruffles associated with of macropinosome formation, thereby

432   leading to a higher number of phages engulfed within each macropinosome (24,66). It is also

433   possible that there is a difference in ruffle size across cell lines leading to a predisposition of

434   some cells to uptake smaller or bigger size phages. A similar relationship between particle size

435   and uptake has been made with nanoparticles, where it was observed that 50 nm size

436   nanoparticles had high rates of uptake, which coincidentally are of similar size as our T3 phages

437   (67–69). It was also shown that the cell type, as well as the particles shape influenced uptake,

438   with disc-shaped particles having higher rates of uptake compared with elongated rod shapes.

439   Again, our T3 phage are coincidentally similarly shaped to the disc-shaped particles (70,71),

440   indicating that the shape of phages may play a role in their uptake; a factor that we cannot rule

441   out from our study. It is intriguing to speculate that much of the research into nanoparticle

442   delivery has converged upon parameters analogous with biology's own naturally-occurring

443   nanoparticles; the bacteriophages.

444

445   We observed, that following the rapid adsorption of phages with *in vitro* cell culture layers, a

446   high proportion of phages were inactivated (Fig. 5b); a phenomenon which has not been

447   previously reported. Our first hypothesis to explain this rapid inactivation is that upon

448   interaction with cell surface features, phages are mechanically triggered to eject their genomes,

449   thereby leading to inactivation (72). This would implicate an increase of phage DNA at the cell

450   surface, which we observed via ddPCR results, along with a concomitant decrease in functional

451   phage particles. Another hypothesis is that the transient and non-specific interactions between

452   the phages and the cell surface features, including glycoproteins, glycolipids, and mucins (73),

453   may physically block or impede the phage such that it is unable to access its host bacterial

454   receptor for plaque quantification, thereby only being detected via ddPCR. Finally, this

455   inactivation could be the result of the degradation of the phage capsid due to enzymes,

456   secretions, or cellular products. Though our negative controls show this is unlikely, as there

457   was no effect of spent cell culture media on phage infectivity (Supplemental Fig. 5). At this

458   stage whilst we cannot conclude the specific mechanisms inducing this rapid loss of phage

459   viability, our results clearly suggest that this rapid inactivation and adsorption to the cell layer

460   may represent a major sink for circulating phages in the body.

461

462   During phage therapy, the cells, organs, and systems of the body play an important role in the

463   efficacy of treatment due to their effect on the sequestration of active phages and limiting

464   accessibility to the site of infection (30,31). It has been proposed that the mononuclear

465   phagocyte system (MPS) is primarily responsible for the filtering and removal of the phages

466   during phage therapy, with the liver and spleen considered the main organs responsible for

467   filtering circulating phages (43,74,75). Recent case studies of phage pharmacokinetics (PK)

468   following intravenous (IV) administration have shown rapid clearance in both humans and

469   animal models, with over > 99% of phages applied removed from circulation within the first

470   few hours (38,76). In an extensive literature review, Dabrowska 2019 (30) noted that the phage

471   titres in the blood immediately following intravenous injection (1-5 minutes) were markedly

472   less than expected hypothetical dilutions. Even when accounting for phage dilutions in the

473   blood or total body volume, phage titres only reached between 0.02% and 0.4% of their

474   predicted titres. This suggests that there is significant and rapid uptake of phages by the organs

475   and cells of the MPS, or alternatively, the rapid adherence and inactivation of phages to the

476   epi- and endothelial cells lining the circulatory system. All the cell lines used in this study;

477   endothelial, epithelial, macrophages or fibroblast, may be in contact with phages at any time

478   during therapy. Our results demonstrate that phages rapidly adhered to and are subsequently

479   internalised by these cells (Fig. 5b). The model we developed in this article (Fig. 6), whilst

480   preliminary, illustrated the potential impact that cell layers play in the inactivation of phages

481   following their delivery to a patient. We suggest that the cell layers of the body are a major

482   sink for phages and that these interactions have unrecognised impacts on phage PK and

483   therapy. If this mechanism is true, then phage most likely display non-linear PK (in addition to

484   non-linear clearance). These results have unrecognised consequences on phage dosing

485   regimens during treatment, implying higher doses and more frequent administrations of phages

486   to patients may be needed in order to reach an optimal phage dose to fight the infection.

487

488   With these new findings on the role of eukaryotic cells in the uptake and inactivation of phages

489   during phage therapy, we hope to help in the design and engineering of treatment for patients

490   and to improve the clinical outcome of phage therapy.

Bichet et al. 2020

Materials and methods

491 **Bacterial stocks and phage stocks**. The bacterial strains used in this study,
493 *Escherichia coli B* strain HER 1024 and *E. coli B* strain W3350, were cultured in lysogeny
494 broth (LB) media (10 g tryptone, 5 g yeast extract, 10 g NaCl, in 1 litre of distilled water
495 [dH$_2$O]) at 37 ºC shaking overnight and used to propagate and titre phages T4, T3 and lambda
496 supplemented with 10 mM CaCl$_2$ and MgSO$_4$. Phages T4, T3 and lambda were cleaned and
497 purified using the Phage on Tap protocol (PoT) (45) and titred up to a concentration of
498 approximately 10^{10} phages per ml. After purification, phages were stored in a final solution of
499 SM Buffer (2.0 g MgSO$_4$·7H$_2$O, 5.8 g NaCl, 50 ml of 1M Tris-HCl pH 7.4, dissolve in 1 litre
500 of dH$_2$O) at 4 ºC.

501 **Endotoxin removal.** For each of the phage samples, endotoxin removal protocol was
502 followed from the Phage on Tap (PoT) protocol (45). Phages lysates were cleaned four times
503 with octanol to remove endotoxins from the lysate.

504 **Cell line stocks.** Seven cell lines were used in this study, all grown at 37 ºC and 5%
505 CO$_2$ and supplemented with 1% penicillin-streptomycin (Life Technologies Australia Pty. Ltd)
506 A549 cells were grown in Ham's F-12K (Kaighn's) (also called F12-K)) (Life Technologies
507 Australia Pty. Ltd) media with 10% Fetal Bovine Serum (FBS) (Life Technologies Australia
508 Pty. Ltd), HUVECs were grown in F12-K media with 20% FBS, HeLa and HT-29 cells were
509 both grown in Dulbecco's Modified Eagle Medium (DMEM) (Life Technologies Australia Pty.
510 Ltd) supplemented with 10% FBS, MDCK-I cells were grown in Modified Eagle Medium
511 (MEM) (Life Technologies Australia Pty. Ltd) with 10% FBS, BJ cells were grown in DMEM
512 media with 10% FBS and 1% sodium pyruvate (Sigma-Aldrich, Australia) and finally the
513 suspension of THP-1 cells were maintained in Roswell Park Memorial Institute (RPMI) 1640
514 media (Life Technologies Australia Pty. Ltd) with 10% FBS. For differentiation, phorbol 12-
515 myristate 13-acetate (PMA) (Sigma-Aldrich, Australia) was added to a final concentration of
516 25 mM and incubated for 48 hours. After incubation PMA supplemented media was removed
517 and cells were further grown in PMA free media for 24 hours to obtain differentiated
518 macrophages. These differentiated cells were stable for up to one week.

519 **Confocal microscopy.** For confocal microscopy experiment, cells were seeded in an
520 IBIDI µ-Slide 8-well glass-bottom slide (DKSH Australia Pty. Ltd) and grown to 80-90%
521 confluency for acquisition. Cells were treated for 20 min with the respective culture media for
522 each cell line with 5% Hoechst 33342 stain, excitation/emission 361/497 nm (Life
523 Technologies Australia Pty. Ltd) and 1% CellMask deep red plasma membrane stain,
524 excitation/emission 649/666 nm (Life Technologies Australia Pty. Ltd). After incubation cells

525 were washed three times with Dulbecco's phosphate-buffered saline (DPBS) 1× and then left

526 in Hank's Balanced Salt Solution (HBSS) with 1% FBS until acquisition. Purified phages were

527 labelled with 1% SYBR-Gold, excitation/emission 495/537 nm (Life Technologies Australia

528 Pty. Ltd) for one hour in the dark at 4 ºC, followed by three washes with HBSS in Amicon-

529 Ultra4 centrifugal unit 100-kDa membrane (Merck Pty. Ltd) to remove excess of stain. The

530 washed phages were resuspended in a final volume of 1 ml in HBSS media. From a 10^9 phage

531 per ml solution, we added 200 µl per well to the cells under the microscope right before the

532 start of the acquisition. Cells were imaged with HC PL APO 63x/1.40 Oil CS2 oil immersion

533 objective by Leica SP8 confocal microscope on inverted stand with a hybrid detector (HyD) in

534 real time. Excitation used for Hoechst 33342 (blue), SYBR-Gold and CellMask deep red was

535 405, 488 and 638 nm; corresponding emission was recorder at 412-462, 508-545 and 648-694

536 nm detection ranges respectively. HyD detector was used in sequential mode to detect the

537 phages, it increases the sensitivity of detection by acquiring the same image multiple times and

538 accumulating the fluorescence signal. All live cell imaging experiments were completed in

539 triplicate (three fields of view per session). One image was acquired every two minutes for two

540 hours. Each field of view was hand-picked depending on the cell confluency and success of

541 staining. Videos were created through post-processing using the FIJI software version 2.0.0-

542 rc-68/1.52f (77). First, the three channels acquired were merged and processed with a Gaussian

543 Blur filter of 0.8. Second, each channel brightness and contrast were enhanced for printing

544 quality. Finally, the time and scale were added to the final movie saved in 12 fps.

545 **Quantification of phages in live cell imaging.** For each live cell experiment, we

546 quantified cells that contained intracellular green fluorescence as indicative of SYBR-Gold

547 labelled phages. Live cell images were acquired every ten minutes were quantified by manual

548 counting the total number of cells in the field of view and the number of cells with intracellular

549 phages to calculate the percentage of cells containing intracellular phages. Results were plotted

550 using the GraphPad Prism version 8.4.2 for macOS GraphPad Software, San Diego, California

551 USA, www.graphpad.com, to show uptake of phages over time.

552 **Clustering analysis.** Univariate clustering was performed using the dynamic

553 programming algorithm in the R package Ckmeans.1d.dp (46).

554 **Flow conditions in microfluidic chip.** A chip mold with 500 µm wide, 350 µm high

555 and 1.3 cm long channels was designed using SolidWorks® 2017. The moulds were 3D-printed

556 using Object Eden360V (Stratasys, USA) with a manufacturer-provided polymer FC720 and

557 surface-salinized in a vacuum desiccator overnight with 20 µl Trichloro(1*H*,1*H*,2*H*,2*H*-

558   perfluorooctyl)silane (Sigma-Aldrich, USA). The microfluidic chips were manufactured via

559   soft-lithography, by casting a 10:1 mixture of Sylgard 184 PDMS and its curing agent (Dowsil,

560   USA) respectively, onto the moulds and were cured at 90 °C until completely solidified (~2

561   hours). The chips were then cut with a surgical knife, gently peeled off, trimmed and their inlet

562   and outlet were punched with 2 mm biopsy punchers (ProSciTech, Australia). Subsequently,

563   the chips were washed in pentane and acetone to remove residual uncured PDMS. Atmospheric

564   plasma generated at 0.65 Torr with high radio frequency was used to bound the PDMS chip to

565   a glass cover slip No. 1.5H (0.170 mm ± 0.005 mm thickness) optimized for confocal

566   microscopy (Marienfeld), for 20 seconds. The microchannel of the assembled microfluidic

567   device were washed with ethanol (80% v/v)-sterilised, UV-sterilised and pre-treated with 1:50

568   MaxGel^{TM} ECM (Sigma-Aldrich) in cold F12-K media for two hours at 37 ºC and 5% CO_2.

569   The microchannel was then washed with F12-K media to remove residual ECM. Schematic

570   and picture of the microdevice is included in supplemental Fig. 2. The channel was seeded with

571   10 µl of HUVECs at a concentration of 5×10^5 cells/ml, which were carefully pipetted through

572   the in port. The seeded chip was incubated statically for 12 hours to allow cell attachment at

573   37 ºC and 5% CO_2. This was followed by perfusing the attached cells with complete media for

574   24 hours at 0.66 µl/min flow rate to establish a confluent cell layer. The cell layer was then

575   perfused with cell culture media supplemented with 20% of FBS for another 24 hr at 8 µl/min

576   to acclimate the cells to the shear stress. Perfusion was mediated by a single-channel syringe

577   pump (New Era Pump Systems, USA) using a 10 ml 21 gauge needled-syringe fitted to Teflon

578   tubes of 1/16" inner diameter and 1/32" outer diameter (Cole-Palmer, USA) that were

579   previously sterilised using ethanol (80% v/v)-sterilised, DPBS and UVs. HUVECs were then

580   stained with nucleus stain, Hoechst 33342 (blue), plasma membrane stain, CellMask (magenta)

581   under static conditions for 20 min. T4 phages labelled with DNA-complexing stain, SYBR-

582   Gold (green) were then added to the chip under 8 µl/min flow rate for either two or 18 hours.

583   After incubation under flow with the phages, the in and out port of the chips were sealed using

584   sterilized-binder paper clips and the chip placed under the microscope. The images were

585   acquired with HC PL APO 63x/1.40 Oil CS2 oil immersion objective on an inverted Leica SP8

586   confocal microscope. A hybrid detector (HyD) was used to visualise phage DNA

587   (excitation/emission 495/537 nm), other channels were acquired with conventional PMT

588   detectors for CellMask (excitation/emission 649/666 nm) and for Hoescht 33342

589   (excitation/emission 361/497 nm).

590   **Image analysis with CellProfiler.** To quantify the fluorescence intensity of SYBR-
591   Gold labelled phages (495 nm wavelength), we used a pipeline created in CellProfiler (60) (see
592   the pipeline used in supplemental data, SD1), allowing us to measure the pixel grey values as
593   a proxy for fluorescence intensity across the image. First, we segmented regions covered by
594   nuclei by applying the IdentifyPrimaryObjects module to the Hoechst channel image. Second,
595   we defined expanded regions around the nuclei for cytoplasmic measurements using the
596   IdentifySecondaryModule with the parameter Distance-N set to 200. Third, we masked out
597   nuclei regions in the of the nuclei SYBR (phages) channel. This is to exclude fluorescence
598   coming from the cell nuclei due to the leaking of the SYBR dye from the phage capsid to the
599   cell nuclei, which would lead to false positive quantification. Finally, the grey values image
600   intensity in the masked SYBR channel and additional parameters of the secondary objects were
601   measured (Supplemental data SD1). Only a single time point at two hours at each field of view
602   was used for the analysis. The number of images analysed for each condition varied, as manual
603   quality control was applied to exclude out of focus and non-analysable fields of view.

604   **Intracellular phages.** For the intracellular phages experiment, cells were plated in T25
605   cm^2 flasks until they reached confluency. For the 18 hours experiment, phages were applied in
606   volumes of 3 ml of media with 10^9 phages/ml per flask and incubated overnight at 37 ºC and
607   5% CO_2. The control flasks were incubated with 3 ml of phage-free media. After the 18 hours
608   incubation, control flasks were incubated with the same phage dilution for 30 seconds. The
609   initial dilution for each flask was collected for quantification. Cells were washed three times
610   with 5 ml of 1 × DPBS to remove non-adherent phages. Next, one ml of 0.5% trypsin was
611   added per flask and incubated at 37 ºC and 5% CO_2 for a few minutes, once cells detached, the
612   cells were resuspended in 5 ml of 1 × DPBS and spun at 1500 rpm for three minutes and washed
613   three times with 5 ml 1 × DPBS to remove any non-adherent phages. After the washes, cells
614   were resuspended in 1 ml of lysis buffer (0.5 M EDTA and 1 M Tris at pH 7.5, complete with
615   dH$_2$O and adjust pH to 8) and left at room temperature for 20 min. After incubation the cells
616   are passed through a 30 G syringe three times to ensure complete cell lysis. The lysis was
617   confirmed by looking at the sample under a microscope.

618   **ddPCR setup.** Digital Droplet Polymerase Chain Reaction (ddPCR) was performed
619   following manufacturer's instructions (Bio-Rad, Australia). A 20 µl reaction was assembled
620   with primers, probe, ddPCR Supermix for probe (Bio-Rad, Australia) and sample. The primer
621   and probe sequence and PCR parameters are shown in supplemental Table 2 - 4. ddPCR
622   reaction mix was then loaded into eight channel disposable droplet generator cartridge (Bio-

Bichet et al. 2020

623 Rad, Australia). 70 µl of droplet generation oil was added to each channel and placed in the
624 Bio-Rad QX200 droplet generator. The droplets were transferred into the deep well 96 well
625 plate (Bio-Rad, Australia), using a multichannel pipette. The plate was then sealed using Bio-
626 Rad plate sealer and then placed in a conventional thermocycler and the PCR product was
627 amplified (supplemental Table 4). After amplification, the plate was loaded into the droplet
628 reader (Bio-Rad, Australia) to quantify the fluorescent droplets. Analysis of the data was
629 performed using the Poisson distribution with QuantaLife software (Bio-Rad, Australia).

630 **PFU quantification**. The Plaque Forming Unit (PFU) assay was performed using LB
631 agar plates where a thin layer of soft LB agar was mixed with one ml of host bacterial culture
632 and the desired dilution of phages was poured on the agar plate. The plate was incubated over-
633 night at 37 ºC before counting the number of plaques formed on the bacterial lawn. The results
634 were calculated in PFU. To obtain the number of inactive phages we subtracted PFU numbers
635 (active phages) from the ddPCR numbers (total number of phages).

636 **Pharmacokinetics Model.** A previously developed PK model in healthy rats was
637 utilized to evaluate the impact of phage inactivation on *in vivo* phage disposition (38). An
638 additional compartment was incorporated to describe the inactivation and reactivation of
639 phages by the epi- and endothelial cells. The rates of inactivation and reactivation was
640 described by first-order rate constant, KD, and was assumed to be constant over time. The
641 differential equations for phage disposition and inactivation were represented by:

642 $$\frac{dA_1(t)}{dt} = -(CL_T + Q_1 + Q_2)\frac{A_1}{V_1}(t) + Q_1\frac{A_2}{V_2}(t) + Q_2\frac{A_3}{V_3}(t) - KD_1A_1(t) + KD_2A_4(t)$$

643 $$\frac{dA_2(t)}{dt} = Q_1\frac{A_1}{V_1}(t) - Q_1\frac{A_2}{V_2}(t)$$

644 $$\frac{dA_3(t)}{dt} = Q_2\frac{A_1}{V_1}(t) - Q_2\frac{A_3}{V_3}(t)$$

645 $$\frac{dA_4(t)}{dt} = KD_1A_1(t) - KD_2A_4(t)$$

646 $$CL_T = \frac{V_{max}}{K_m + \frac{A_1}{V_1}}$$

647 where

648 Q_1 = inter-compartmental clearance 1 (mL/h/Rat).

649 Q_2 = inter-compartmental clearance 2 (mL/h/Rat).

650 V_1 = Volume of distribution of the central compartment (mL/Rat).

651 V_2 = Volume of distribution of the peripheral compartment 1 (mL/Rat).

652 V_3 = Volume of distribution of the peripheral compartment 2 (mL/Rat).

26

Bichet et al. 2020

653 k_m = Phage titre that produces 50% of the maximal elimination rate of the system (PFU/mL/Rat).

654 V_{max} = Maximum elimination rate (PFU/h/Rat).

655 KD_1 = Inactivation rate constant (1/h).

656 KD_2 = Reactivation rate constant (1/h).

657 Deterministic was performed using model-predicted median PK parameters in rats without

658 inter-individual variability and random unexplained variability (Supplementary table 5).

659 Inactivation rate constant was determined using the ddPCR results as described in

660 Supplementary table 5. First order for the 30 seconds graph is of 1415 1/h/rat and for the 18

661 hours the first order is of 0.358 1/h/rat calculated from the ddPCR data. Reactivation rate

662 constant was fixed to 0. Deterministic simulations were performed in R using mrgsolve

663 (version 0.10.4) (38,78).

664

665

Authors participation

Conceptualization: MCB, JJB; Methodology: MCB, WHC, WR, AO, LAF, CAH, YWL; Formal Analysis: MCB, JJB; Investigation: MCB; Resources: JJB; Writing – Original Draft Preparation: MCB, RP, JJB; Writing – Review and Editing: all authors contributed; Supervision and Funding Acquisition: JJB

691

Bichet et al. 2020

692

References:

694

695   1.   Rohwer F, Segall AM. In retrospect: A century of phage lessons. Nature. 2015;528(7580):46–8.

697   2.   Hatfull GF. Dark Matter of the Biosphere: the Amazing World of Bacteriophage Diversity. J Virol. 2015 Aug;89(16):8107–10.

699   3.   Rohwer F. Global phage diversity. Cell Press. 2003;113:141.

700   4.   Clokie MRJ, Millard AD, Letarov A V, Heaphy S. Phages in nature. Bacteriophage. 2011;1(1):31–45.

702   5.   Breitbart M, Hewson I, Felts B, Mahaffy JM, Nulton J, Salamon P, et al. Metagenomic Analyses of an Uncultured Viral Community from Human Feces. J Bacteriol. 2003;185(20):6220–3.

705   6.   Manrique P, Bolduc B, Walk ST, Van Der Oost J, De Vos WM, Young MJ. Healthy human gut phageome. Proc Natl Acad Sci. 2016;113(37):10400–5.

707   7.   Shkoporov AN, Hill C. Bacteriophages of the Human Gut: The "Known Unknown" of the Microbiome. Cell Host and Microbe. 2019;Elsevier 25:195–209.

709   8.   Nguyen S, Baker K, Padman BS, Patwa R, Dunstan RA, Weston TA, et al. Bacteriophage transcytosis provides a mechanism to cross epithelial cell layers. MBio. 2017;8(6).

712   9.   Sender R, Fuchs S, Milo R. Are We Really Vastly Outnumbered? Revisiting the Ratio of Bacterial to Host Cells in Humans. Cell. 2016; Cell Press;164:337–40.

714   10.   Barr JJ. A bacteriophages journey through the human body. Immunol Rev. 2017;279(1):106–22.

716   11.   Górski A, Wazna E, Dąbrowska BW, Dąbrowska K, Świtała-Jeleń K, Międzybrodzki R. Bacteriophage translocation. FEMS Immunol Med Microbiol. 2006;46(3):313–9.

718   12.   Ghose C, Ly M, Schwanemann LK, Shin JH, Atab K, Barr JJ, et al. The Virome of Cerebrospinal Fluid: Viruses Where We Once Thought There Were None. Front Microbiol. 2019 Sep;10.

721   13.   Międzybrodzki R, Kłak M, Jonczyk-Matysiak E, Bubak B, Wójcik A, Kaszowska M, et al. Means to facilitate the overcoming of gastric juice barrier by a therapeutic staphylococcal bacteriophage A5/80. Front Microbiol. 2017 Mar;8:1–11.

724   14.   Geier MR, Trigg ME, Merril CR. Fate of bacteriophage lambda in Non-immune germ-

Bichet et al. 2020

725   free mice. Nature. 1973;246(5430):221–3.

726 15. Huh H, Wong S, St. Jean J, Slavcev R. Bacteriophage interactions with mammalian
727   tissue: Therapeutic applications. Adv Drug Deliv Rev. 2019;145:4–17.

728 16. Dabrowska K, Switała-Jelen K, Opolski A, Weber-Dabrowska B, Gorski A. A review:
729   Bacteriophage penetration in vertebrates. J Appl Microbiol. 2005;98(1):7–13.

730 17. Dor-On E, Solomon B. Targeting glioblastoma via intranasal administration of Ff
731   bacteriophages. Front Microbiol. 2015;6.

732 18. Srivastava AS, Chauhan DP, Carrier E. In utero detection of T7 phage after systemic
733   administration to pregnant mice. BioTechniques. 2004; 37.

734 19. Gorski A, Dabrowska K, Switala-Jele K, Nowaczyk M, Weber-Dabrowska B,
735   Boratynski J, et al. New insights into the possible role of bacteriophages in host
736   defense and disease. Med Immunol. 2003 Feb;2:2.

737 20. Karimi M, Mirshekari H, Moosavi Basri SM, Bahrami S, Moghoofei M, Hamblin MR.
738   Bacteriophages and phage-inspired nanocarriers for targeted delivery of therapeutic
739   cargos. Adv Drug Deliv Rev. 2016;106:45–62.

740 21. Handley SA, Thackray LB, Zhao G, Presti R, Miller AD, Droit L, et al. Pathogenic
741   simian immunodeficiency virus infection is associated with expansion of the enteric
742   virome. Cell. 2012;151(2):253–66.

743 22. Lehti TA, Pajunen MI, Skog MS, Finne J. Internalization of a polysialic acid-binding
744   Escherichia coli bacteriophage into eukaryotic neuroblastoma cells. Nat Commun.
745   2017;8(1).

746 23. Tao P, Mahalingam M, Marasa BS, Zhang Z, Chopra AK, Rao VB. In vitro and in
747   vivo delivery of genes and proteins using the bacteriophage T4 DNA packaging
748   machine. Proc Natl Acad Sci. 2013 Apr;110(15):5846–51.

749 24. Kerr MC, Teasdale RD. Defining Macropinocytosis. Traffic. 2009 Apr;10(4):364–71.

750 25. Gordillo Altamirano FL, Barr JJ. Phage Therapy in the Postantibiotic Era. Clin
751   Microbiol Rev. 2019;32(2):1–25.

752 26. Merril CR, Scholl D, Adhya SL. The prospect for bacteriophage therapy in Western
753   medicine. Nat Rev Drug Discov. 2003 Jun;2(6):489–97.

754 27. Kutter E, De Vos D, Gvasalia G, Alavidze Z, Gogokhia L, Kuhl S, et al. Phage
755   Therapy in Clinical Practice: Treatment of Human Infections. Curr Pharm Biotechnol.
756   2010 Feb;11(1):69–86.

757 28. Abedon ST, Kuhl SJ, Blasdel BG, Kutter EM. Phage treatment of human infections.

758   Bacteriophage. 2011;1(2):66–85.

759   29.   Matsuzaki S, Uchiyama J. Phage Pharmacokinetics: Relationship with Administration

760   Route. In: Phage Therapy: A Practical Approach. Springer International Publishing.

761   2019;43–57.

762   30.   Dąbrowska K. Phage therapy: What factors shape phage pharmacokinetics and

763   bioavailability? Systematic and critical review. 2019;Med Res Rev 39(5):2000–25.

764   31.   Dąbrowska K, Abedon ST. Pharmacologically Aware Phage Therapy:

765   Pharmacodynamic and Pharmacokinetic Obstacles to Phage Antibacterial Action in

766   Animal and Human Bodies. Microbiol Mol Biol Rev. 2019;83(4):1–25.

767   32.   Payne RJH, Jansen VAA. Understanding bacteriophage therapy as a density-dependent

768   kinetic process. J Theor Biol. 2001 Jan;208(1):37–48.

769   33.   Payne RJH, Jansen VAA. Phage therapy: The peculiar kinetics of self-replicating

770   pharmaceuticals. Clinical Pharmacology and Therapeutics. 2000;68:225–30.

771   34.   Hoffmann M. Animal Experiments on Mucosal Passage and Absorption Viraemia of

772   T3 Phages after Oral, Trachéal and Rectal Administration. Zentralblatt fur Bakteriol

773   Parasitenkunde, Infekt und Hyg. 1965;198(4):371–90.

774   35.   Hildebrand GJ, Wolochow H. Translocation of Bacteriophage Across the Intestinal

775   Wall of the Rat. Exp Biol Med. 1962 Jan;109(1):183–5.

776   36.   Keller R, Engley FB. Fate of Bacteriophage Particles Introduced into Mice by Various

777   Routes. Exp Biol Med. 1958 Jul;98(3):577–80.

778   37.   Sweere JM, Belleghem JD Van, Ishak H, Bach MS, Popescu M, Sunkari V, et al. of

779   bacterial infection. 2019 Mar;9691.

780   38.   Lin Y-W, Kyung Chang RY, Rao GG, Jermain B, Han M-L, Zhao J, et al.

781   Pharmacokinetics/pharmacodynamics of antipseudomonal bacteriophage therapy in

782   rats: A Proof-of-Concept study. Clin Microbiol Infect. 2020 May.

783   39.   Doub JB, Ng VY, Johnson AJ, Slomka M, Fackler J, Horne B, et al. Salvage

784   Bacteriophage Therapy for a Chronic MRSA Prosthetic Joint Infection. Antibiotics.

785   2020;9:241.

786   40.   Hodyra-Stefaniak K, Lahutta K, Majewska J, Kaźmierczak Z, Lecion D, Harhala M, et

787   al. Bacteriophages engineered to display foreign peptides may become short-

788   circulating phages. Microb Biotechnol. 2019 Jul;12(4):730–41.

789   41.   Carroll-Portillo A, Lin HC. Bacteriophage and the innate immune system: Access and

790   signaling. Microorganisms. 2019;7(12):1–11.

Bichet et al. 2020

791   42.   Van Belleghem JD, Dąbrowska K, Vaneechoutte M, Barr JJ, Bollyky PL. Interactions

792   between bacteriophage, bacteria, and the mammalian immune system. Viruses. 2019

793   Jan;11(1).

794   43.   Hodyra-Stefaniak K, Miernikiewicz P, Drapała J, Drab M, Jonczyk-Matysiak E,

795   Lecion D, et al. Mammalian Host-Versus-Phage immune response determines phage

796   fate in vivo. Sci Rep. 2015 Oct;5(1):1–13.

797   44.   Sweere JM, Van Belleghem JD, Ishak H, Bach MS, Popescu M, Sunkari V, et al.

798   Bacteriophage trigger antiviral immunity and prevent clearance of bacterial infection.

799   Science. 2019 Mar;363(6434).

800   45.   Bonilla N, Rojas MI, Netto Flores Cruz G, Hung S-H, Rohwer F, Barr JJ. Phage on

801   tap–a quick and efficient protocol for the preparation of bacteriophage laboratory

802   stocks. PeerJ. 2016;4:e2261.

803   46.   Wang H, Song M. Ckmeans.1d.dp: Optimal k-means clustering in one dimension by

804   dynamic programming. R J. 2011;3(2):29–33.

805   47.   Kim HJ, Li H, Collins JJ, Ingber DE. Contributions of microbiome and mechanical

806   deformation to intestinal bacterial overgrowth and inflammation in a human gut-on-a-

807   chip. Proc Natl Acad Sci. 2016;113(1):e7–15.

808   48.   Kim HJ, Huh D, Hamilton G, Ingber DE. Human Gut-on-a-Chip inhabited by

809   microbial flora that experiences intestinal peristalsis-like motions and flow. R Soc

810   Chem. 2012;12:2165–74.

811   49.   Navabi N, McGuckin MA, Linden SK. Gastrointestinal Cell Lines Form Polarized

812   Epithelia with an Adherent Mucus Layer when Cultured in Semi-Wet Interfaces with

813   Mechanical Stimulation. PLoS One. 2013;8(7).

814   50.   Kim L, Toh YC, Voldman J, Yu H. A practical guide to microfluidic perfusion culture

815   of adherent mammalian cells. Lab Chip. 2007;7(6):681–94.

816   51.   Thuenauer R, Rodriguez-Boulan E, Rümer W. Microfluidic approaches for epithelial

817   cell layer culture and characterisation. Analyst. 2014;139(13):3206–18.

818   52.   Son Y. Determination of shear viscosity and shear rate from pressure drop and flow

819   rate relationship in a rectangular channel. Polymer (Guildf). 2007 Jan;48(2):632–7.

820   53.   Chin WH, Barr JJ. Phage research in 'organ-on-chip' devices. Microbiol Aust. 2019

821   Mar.

822   54.   Barr JJ, Auro R, Sam-Soon N, Kassegne S, Peters G, Bonilla N, et al. Subdiffusive

823   motion of bacteriophage in mucosal surfaces increases the frequency of bacterial

824   encounters. Proc Natl Acad Sci. 2015;112(44):13675–80.

825   55.   Yum K, Hong SG, Healy KE, Lee LP. Physiologically relevant organs on chips.

826   Biotechnol J. 2014 Jan;9(1):16–27.

827   56.   Wang C, Lu H, Alexander Schwartz M. A novel in vitro flow system for changing

828   flow direction on endothelial cells. J Biomech. 2012;45(7):1212–8.

829   57.   Abaci HE, Shen YI, Tan S, Gerecht S. Recapitulating physiological and pathological

830   shear stress and oxygen to model vasculature in health and disease. Sci Rep. 2014

831   May;4(1):1–9.

832   58.   Park JY, White JB, Walker N, Kuo CH, Cha W, Meyerhoff ME, et al. Responses of

833   endothelial cells to extremely slow flows. Biomicrofluidics. 2011 Jun;5(2):022211.

834   59.   Davies PF, Spaan JA, Krams R. Shear stress biology of the endothelium. Ann Biomed

835   Eng. 2005 Dec;33:1714–8.

836   60.   McQuin C, Goodman A, Chernyshev V, Kamentsky L, Cimini BA, Karhohs KW, et

837   al. CellProfiler 3.0: Next-generation image processing for biology. PLoS Biol. 2018;

838   61.   Hosta-Rigau L, Städler B. Shear stress and its effect on the interaction of myoblast

839   cells with nanosized drug delivery vehicles. Mol Pharm. 2013 Jul;10(7):2707–12.

840   62.   Han J, Zern BJ, Shuvaev V V., Davies PF, Muro S, Muzykantov V. Acute and chronic

841   shear stress differently regulate endothelial internalization of nanocarriers targeted to

842   platelet-endothelial cell adhesion molecule-1. ACS Nano. 2012 Oct;6(10):8824–36.

843   63.   Canton J. Macropinocytosis: New Insights Into Its Underappreciated Role in Innate

844   Immune Cell Surveillance. Front Immunol. 2018;9:2286.

845   64.   Talman L, Agmon E, Peirce SM, Covert MW. Multiscale models of infection. Vol. 11,

846   Current Opinion in Biomedical Engineering. 2019;Elsevier 11:102–8.

847   65.   Bodner K, Melkonian AL, Barth AIM, Kudo T, Tanouchi Y, Covert MW. Engineered

848   Fluorescent E. coli Lysogens Allow Live-Cell Imaging of Functional Prophage

849   Induction Triggered inside Macrophages. Cell Syst. 2020;10(3):254-264.

850   66.   Swanson JA, Watts C. Macropinocytosis. Trends in Cell Biology. 1995;Elsevier

851   Current Trends 5:424–8.

852   67.   Lu F, Wu S-H, Hung Y, Mou C-Y. Size Effect on Cell Uptake in Well-Suspended,

853   Uniform Mesoporous Silica Nanoparticles. Small. 2009; 5(12):1408–13.

854   68.   Yin Win K, Feng SS. Effects of particle size and surface coating on cellular uptake of

855   polymeric nanoparticles for oral delivery of anticancer drugs. Biomaterials. 2005;

856   26(15):2713–22.

Bichet et al. 2020

857　69.　Zhu J, Liao L, Zhu L, Zhang P, Guo K, Kong J, et al. Size-dependent cellular uptake
858　　　　efficiency, mechanism, and cytotoxicity of silica nanoparticles toward HeLa cells.
859　　　　Talanta. 2013;107:408–15.

860　70.　Agarwal R, Singh V, Jurney P, Shi L, Sreenivasan S V., Roy K. Mammalian cells
861　　　　preferentially internalize hydrogel nanodiscs over nanorods and use shape-specific
862　　　　uptake mechanisms. Proc Natl Acad Sci. 2013 Oct;110(43):17247–52.

863　71.　Hsiao I-L, Gramatke AM, Joksimovic R, Sokolowski M, Gradzielski M, Haase A. Size
864　　　　and Cell Type Dependent Uptake of Silica Nanoparticles. J Nanomed Nanotechnol.
865　　　　2014;05(06).

866　72.　Kellermayer MSZ, Vörös Z, Csík G, Herényi L. Forced phage uncorking: viral DNA
867　　　　ejection triggered by a mechanically sensitive switch. Nanoscale. 2018;10:1898.

868　73.　Barr JJ, Auro R, Furlan M, Whiteson KL, Erb ML, Pogliano J, et al. Bacteriophage
869　　　　adhering to mucus provide a non-host-derived immunity. Proc Natl Acad Sci.
870　　　　2013;110(26):10771–6.

871　74.　Geier MR, Trigg ME, Merril CR. Fate of bacteriophage lambda in Non-immune germ-
872　　　　free mice. Nature. 1973;246(5430):221–3.

873　75.　Merril CR, Biswas B, Carlton R, Jensen NC, Creed GJ, Zullo S, et al. Long-circulating
874　　　　bacteriophage as antibacterial agents. Proc Natl Acad Sci. 1996 Apr;93(8):3188–92.

875　76.　Schooley RT, Biswas B, Gill JJ, Hernandez-Morales A, Lancaster J, Lessor L, et al.
876　　　　Development and use of personalized bacteriophage-based therapeutic cocktails to
877　　　　treat a patient with a disseminated resistant Acinetobacter baumannii infection.
878　　　　Antimicrob Agents Chemother. 2017;61(10):1–14.

879　77.　Schindelin J, Arganda-Carreras I, Frise E, Kaynig V, Longair M, Pietzsch T, et al. Fiji:
880　　　　an open-source platform for biological-image analysis. Nat Methods. 2012;9(7).

881　78.　Bunn A, Korpela M. A dendrochronology program library in R (dplR).
882　　　　Dendrochronologia. 2018 Jul;26(2):115-24.

883